# Mesoscale bicontinuous networks in self-healing hydrogels delay fatigue fracture

Xueyu Li, Kunpeng Cui, Tao Lin Sun, Lingpu Meng, Chengtao Yu, Liangbin Li, Costantino Creton, Takayuki Kurokawa, Jian Ping Gong

# Mesoscale bicontinuous networks in self-healing hydrogels delay fatigue fracture

Xueyu Li[a], Kunpeng Cui[b], Tao Lin Sun[a,c,d], Lingpu Meng[e,f,g], Chengtao Yu[h], Liangbin Li[e,f,g], Costantino Creton[a,i], Takayuki Kurokawa[a,c], and Jian Ping Gong[a,b,c,1]

[a]Global Station for Soft Matter, Global Institution for Collaborative Research and Education, Hokkaido University, 001-0021 Sapporo, Japan; [b]Institute for Chemical Reaction Design and Discovery, Hokkaido University, 001-0021 Sapporo, Japan; [c]Faculty of Advanced Life Science, Hokkaido University, 001-0021 Sapporo, Japan; [d]South China Advanced Institute for Soft Matter Science and Technology, South China University of Technology, 510640 Guangzhou, China; [e]National Synchrotron Radiation Laboratory, University of Science and Technology of China, 230026 Hefei, China; [f]Anhui Provincial Engineering Laboratory of Advanced Functional Polymer Film, University of Science and Technology of China, 230026 Hefei, China; [g]Chinese Academy of Sciences Key Laboratory of Soft Matter Chemistry, University of Science and Technology of China, 230026 Hefei, China; [h]Graduate School of Life Science, Hokkaido University, 060-0810 Sapporo, Japan; and [i]Laboratoire Sciences et Ingénierie de la Matière Molle, École Supérieure de Physique et de Chimie Industrielles de la Ville de Paris (ESPCI), Université de Recherche Paris-Sciences-et-Lettres (PSL), Sorbonne Université, CNRS, F-75005 Paris, France

Edited by Zhigang Suo, Harvard University, Cambridge, MA, and approved February 26, 2020 (received for review January 7, 2020)

**Load-bearing biological tissues, such as muscles, are highly fatigue-resistant, but how the exquisite hierarchical structures of biological tissues contribute to their excellent fatigue resistance is not well understood. In this work, we study antifatigue properties of soft materials with hierarchical structures using polyampholyte hydrogels (PA gels) as a simple model system. PA gels are tough and self-healing, consisting of reversible ionic bonds at the 1-nm scale, a cross-linked polymer network at the 10-nm scale, and bicontinuous hard/soft phase networks at the 100-nm scale. We find that the polymer network at the 10-nm scale determines the threshold of energy release rate $G_0$ above which the crack grows, while the bicontinuous phase networks at the 100-nm scale significantly decelerate the crack advance until a transition $G_{tran}$ far above $G_0$. In situ small-angle X-ray scattering analysis reveals that the hard phase network suppresses the crack advance to show decelerated fatigue fracture, and $G_{tran}$ corresponds to the rupture of the hard phase network.**

fatigue resistance | hierarchical structure | phase network | crack growth | affine deformation

Suppression and deceleration of crack growth under cyclic loading are observed in load-bearing biological tissues, such as muscles and bones (1, 2). Such antifatigue ability of biotissues, which is essential for their function, should be related to their exquisitely organized hierarchical structures at different scales. For example, skeletal muscles, having a hierarchical structure ranging from folded proteins through noncovalent bonds at the molecular scale to muscle fibers at the micrometer scale (3, 4), sustain repeated stretching and contraction over 1 billion cycles (5, 6) and crack propagation is suppressed even to an injury (7). On the other hand, common synthetic soft materials are unstructured and usually exhibit poor fatigue resistance as a result of strain concentration at crack tip (8) or polymer network imperfection (9). For example, synthetic hydrogels could be made tough and self-healing by introducing noncovalent bonds to dissipate energy (10, 11), but these tough hydrogels show poor fatigue resistance (12, 13). Above a threshold of energy release rate $G_0$, the crack grows rapidly with the fatigue cycle. It has been revealed that the threshold $G_0$ is only determined by the primary network structure of the materials, which depends on chemical cross-linking density (13–16). The antifatigue properties of soft materials are found to be effectively improved by introducing additional structures to the primary network structure, such as crystals (17–19), composites (20–22), ordered folded units (23, 24), and so on. These results suggest that hierarchical structures may contribute to reduce the strain/stress concentration at the crack tip and hence be beneficial for fatigue resistance in these kinds of soft materials. However, the mechanism by which well-designed hierarchical structures at microscopic level can mitigate or suppress crack advance remains poorly understood.

In this work we attempt to elucidate the role of hierarchical structures on the fatigue resistance of self-healing soft materials, focusing on the mechanism of suppression of crack advance and delayed antifatigue-fracture. We chose the recently developed self-healing polyampholyte hydrogels (PA gels) (25–27) as model materials. These PA gels, containing ionic bonds at the 1-nm scale, a cross-linked polymer network at the 10-nm scale, and isotropic bicontinuous hard/soft phase networks at the 100-nm scale (Fig. 1), exhibit a multiscale response to loads and dissipate large amounts of energy to show a very high toughness (28). Such hierarchical structures make the PA gels good candidates as a simple model system to study the effect of hierarchical structures on the fatigue behavior of self-healing materials containing abundant noncovalent bonds. By combining fatigue measurement and time-resolved synchrotron radiation small-angle X-ray scattering (SAXS) we discovered that, upon fatigue cycling, the bicontinuous phase networks in PA gels form a transient oriented structure to induce a pronounced crack blunting and crack

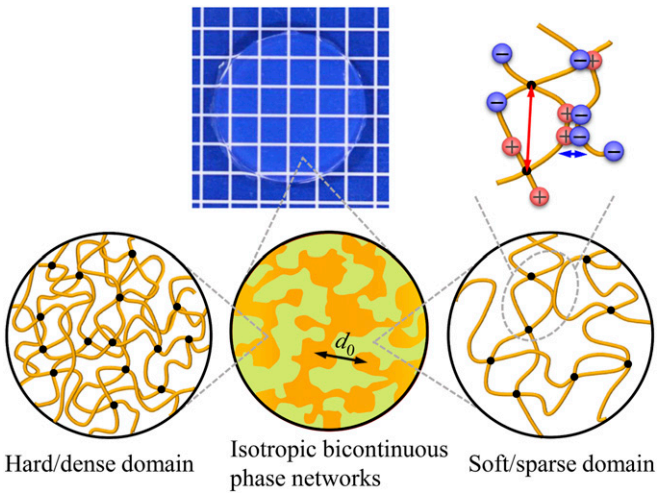


**Fig. 1.** Illustration for hierarchical structures in PA gels. PA gels are composed of hierarchical structures containing ionic bonds (sacrificial bond) at the 1-nm scale (indicated by blue arrow), cross-linked polymer network with mesh size at the 10-nm scale (indicated by red arrow), and bicontinuous hard/soft phase networks with mesh size at $d_0$ ~100-nm scale (indicated by black arrow).

deceleration effect, resulting in an extremely slow mode of crack growth above the energy release rate threshold $G_0$. This mode is maintained until the energy release rate exceeds a transition $G_{tran}$ that is several times higher than $G_0$. Above $G_{tran}$, the stress-carrying hard phase network ruptures, resulting in an abrupt jump of crack growth to a fast mode. Thus, the 100-nm-scale bicontinuous hard/soft phase networks substantially decelerate the fatigue fracture and remarkably enhance the fatigue resistance of the tough hydrogels.

## Results and Discussion

**Tuning Hierarchical Structures in Self-Healing Hydrogels.** PA gels used in this study were obtained from a chemically cross-linked copolymer consisting of the oppositely charged monomers sodium *p*-styrenesulfonate (NaSS) and methyl chloride quaternized *N,N*-dimethylamino ethylacrylate (DMAEA-Q) (*SI Appendix*, Fig. S1). The opposite charges on the polymer chains form ionic bonds when the small counter ions ($Na^+$ and $Cl^-$) are removed from the PA gels by dialysis of the samples in pure water. The formation of these ionic bonds induces local aggregation of the polymers, and as a result the gels form a dense hard phase and sparse soft phase interconnected at ~100-nm scale (28). Such a structure acts as bicontinuous hard/soft phase networks. The primary network structure in the 10-nm scale depends on the formulation of monomer and cross-linker concentrations in precursor solution, which controls the cross-linking density of the network from the chemical cross-linker and from trapped polymer entanglement, while the contrast and the size of the hard/soft phase networks depend on the primary network structure as well as the temperature at which the dialysis of the PA gels was performed. In this work, we adopted the samples with the same primary network structure but different phase network structure. For this purpose, the samples were synthesized from the same formulation but dialyzed at different temperatures (see *SI Appendix* for sample preparation). The samples are coded as PA-$T_{dial}$, where $T_{dial}$ (5 °C, 30 °C, and 60 °C) stands for the dialysis temperature. The water content and thickness of these samples were ~46 wt % and ~1.64 mm, respectively, independent of $T_{dial}$.

First, we show the structure and mechanical behavior of these PA gels. As shown in Fig. 2*A*, SAXS images of the samples show an isotropic ring and a peak in one-dimensional (1D) scattering profiles, attributed to the bicontinuous phase networks consisting of a soft network (with a low modulus) and a hard network (with a high modulus) (28, 29). The intensity of the peak $I_m$ significantly increases with the increase of $T_{dial}$. Furthermore, the average mesh size of the phase networks, related to the periodicity of the hard and soft phases ($d_0$), increases slightly with the increase of $T_{dial}$ (Fig. 2*D*). These results indicate that a higher dialysis temperature induces stronger phase separation, to form bicontinuous networks with a higher density contrast and slightly larger size. Such a temperature effect should be attributed to an enhanced hydrophobic interaction of the polymers at high temperature. The tensile behaviors of gels with different phase network structure exhibit little difference (Fig. 2*B*).

**Deformation of Mesoscale Bicontinuous Phase Networks under Tensile Test.** The deformation of the phase networks of PA gels shows three regimes, as observed by in situ time-resolved SAXS during a uniaxial tensile test (*SI Appendix*, Fig. S3 and Fig. 2*C*). In regime I, the bicontinuous networks deform affinely, assuming incompressibility. That is, the mesh size of the phase networks in the parallel ($d_{//}$) and perpendicular ($d_\perp$) direction obeys $d_{//}/d_0 = \lambda$ and $d_\perp/d_0 = \lambda^{-1/2}$, respectively, with the global elongation ratio $\lambda$. As previously demonstrated (28), the loading–unloading curves exhibit a fully recoverable hysteresis in the affine deformation regime. During loading, the ionic bonds break, and the polymer chains in a globule conformation are unfolded, contributing to energy dissipation responsible for toughening the materials. During unloading, the entropic elasticity drives the polymer chains back to their original globule conformation. After a certain waiting time, the temporary ionic bonds formed in the deformed state dissociate and the original ionic bonds in the undeformed state are reformed to show full recovery of structure and properties. In regime II, $d_\perp/d_0$ decreases slowly and deviates from affine deformation. In this regime, the first loading sample softens but fully shrinks back to its original size after a sufficiently long waiting time, which indicates that the hard phase network ruptures, while the soft phase network stays intact, providing the entropic restoring force (28). In regime III, $d_\perp/d_0$ increases slightly with $\lambda$, and the failure of the whole sample occurs soon thereafter, by rupture of the soft phase network. We observe that the maximum stretch ratio for the affine-like deformation of the phase network, $\lambda_{affine}$, slightly increases with the dialysis temperature of the samples (Fig. 2*D*). This order is consistent with the change in the degree of phase contrast and mesh size $d_0$ of the two networks that both increase with dialysis temperature.

**Suppressed Crack Advance and Delayed Fatigue Fracture.** Then, we explored the cyclic fatigue behavior in uniaxial tension of these PA samples with differently tuned bicontinuous phase networks. The fatigue experiments were performed using prenotched samples in the pure shear geometry (Fig. 3*C*, *Inset*) in a humidity-controlled box (*SI Appendix*, Fig. S2*A*), following the method by Suo and coworkers (30). The cyclic fatigue behaviors are found to be sensitively depended on the relationship between the maximum stretch ratio $\lambda_{max}$ applied in the cyclic fatigue test and the maximum affine deformation ratio $\lambda_{affine}$ observed in the tensile test. As shown in Fig. 3 *A–C* for the PA-30 as a representative, we observe a striking difference for $\lambda_{max} = 2.94$ ($<\lambda_{affine}$) and $\lambda_{max} = 3.19$ ($>\lambda_{affine}$). For $\lambda_{max} = 2.94$, a blunt crack tip forms progressively (Fig. 3*A*). The crack length $c$ initially increases fast, but crack growth slows down soon to a much slower crack propagation rate with increasing cycle $N$. The average crack advance rate at steady state $\Delta c/\Delta N$ is extremely small ($\Delta c/\Delta N = 0.028$ μm per cycle; red sphere in Fig. 3*C*). On the other hand, for $\lambda_{max} = 3.19$, a relatively sharp crack tip is observed (Fig. 3*B*), and the crack length $c$ always increases fast with the number of cycles $N$. The samples failed after only 800 cycles,

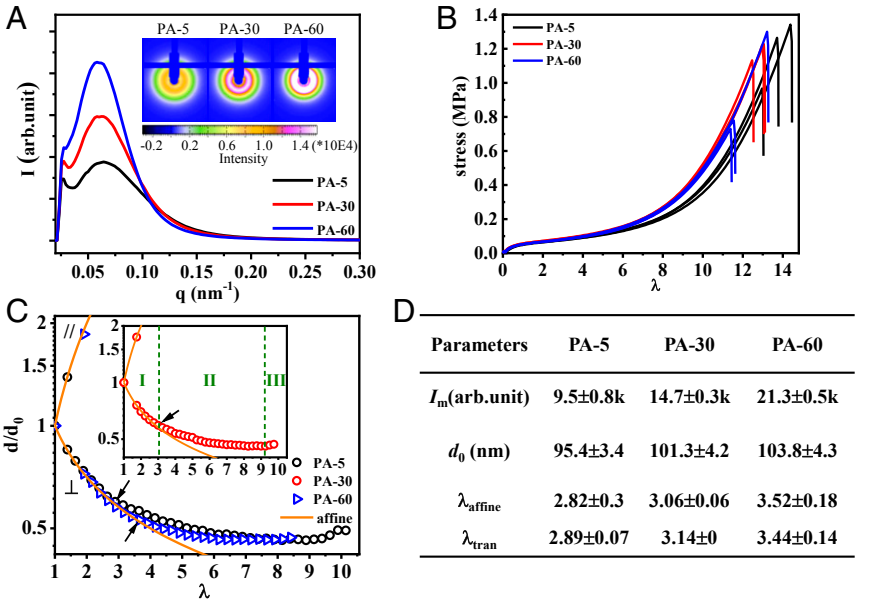


| Parameters | PA-5 | PA-30 | PA-60 |
|---|---|---|---|
| $I_m$(arb.unit) | 9.5±0.8k | 14.7±0.3k | 21.3±0.5k |
| $d_0$ (nm) | 95.4±3.4 | 101.3±4.2 | 103.8±4.3 |
| $\lambda_{affine}$ | 2.82±0.3 | 3.06±0.06 | 3.52±0.18 |
| $\lambda_{tran}$ | 2.89±0.07 | 3.14±0 | 3.44±0.14 |

**Fig. 2.** Structure and tensile behavior of PA gels used in this study. (*A*) The 1D SAXS profiles of undeformed gels dialyzed at various temperatures $T_{dial}$, coded as PA-$T_{dial}$. (*Inset*) The 2D SAXS images. (*B*) Tensile behaviors of the gels. (*C*) Phase network deformation ratio in parallel ($d_{//}/d_0$) and perpendicular ($d_{\perp}/d_0$) directions versus global elongation ratio λ. The orange lines stand for the affine deformation of the phase networks. The maximum affine deformation $\lambda_{affine}$ for each sample is indicated by arrows. (*Inset*) For clarity, the data of PA-30 are shown, and three deformation regimes are marked. (*D*) Summary of SAXS peak intensity $I_m$, average phase network mesh size $d_0$, maximum affine elongation ratio of phase networks $\lambda_{affine}$ in tensile test, and critical elongation ratio of fatigue test for fast crack growth, $\lambda_{tran}$ (extracted from Fig. 3*D*). a.u., arbitrary unit.

showing a fast crack propagation rate $\Delta c/\Delta N$ (~59 μm per cycle; red diamond in Fig. 3*C*), three orders of magnitude larger than that of the sample tested at $\lambda_{max} = 2.94$.

We observed similar behaviors for PA-5 where the crack length $c$ also initially increased fast, slowed down, and finally hardly increased at a representative elongation ratio $\lambda_{max} = 2.54$ ($<\lambda_{affine}$), while it increased rapidly until fracture of the whole sample at $\lambda_{max} = 2.94$ ($>\lambda_{affine}$) (*SI Appendix*, Fig. S4*A*). PA-60 also exhibits the same suppression of crack advance (crack blunting) and fast crack extension behavior at $\lambda_{max} = 2.94$ ($<\lambda_{affine}$) and $\lambda_{max} = 3.84$ ($>\lambda_{affine}$), respectively (*SI Appendix*, Fig. S4*B*).

The $\lambda_{max}$ dependences of the crack growth rate $\Delta c/\Delta N$ for the three materials with different $T_{dial}$ are shown in Fig. 3*D*. All three of the materials show no measurable crack growth over 40,000 cycles below a threshold value of $\lambda_{max}$ defined here as $\lambda_0$. Above $\lambda_0$, the crack started to grow slowly at steady state. A transition of $\Delta c/\Delta N$ from a slow crack growth mode to a fast crack growth mode occurred at a value of $\lambda_{max}$ that we define as $\lambda_{tran}$. Specifically, the three materials show a similar threshold value $\lambda_0$ ~2, and the crack advances very slowly ($\Delta c/\Delta N < 0.1$ μm/cycle) at $\lambda_0 < \lambda_{max} < \lambda_{tran}$, as a result of crack blunting. At $\lambda_{tran} = 2.89 \pm 0.07$, $3.14 \pm 0$, and $3.44 \pm 0.14$ (*SI Appendix*, Fig. S5) for PA-5, 30, and 60, respectvely, a jump of crack growth rate $\Delta c/\Delta N$ to the fast mode ($\Delta c/\Delta N > 10$ μm/cycle) occurs (Fig. 3*D*). The values of $\lambda_{tran}$ are almost coincident with the values of $\lambda_{affine}$ observed by the tensile test (Fig. 2*D*). This result suggests that $\lambda_{tran}$ corresponds to the limit of affine deformation ratio for the fatigue test, and that the high fatigue resistance is achieved when the hard phase network is intact.

We consider that the coincidence of $\lambda_{tran}$ and $\lambda_{affine}$ is due to two reasons. One is that the rupture of the hard phase network occurs at similar elongation ratio λ in the fatigue test (in 10 mm × 50 mm pure shear geometry) and in the tensile test (in 16-mm × 7.5-mm strip geometry). In fact, the stress–elongation curves of the uniaxial tensile tests in pure shear geometry and in strip geometry almost overlap with each other at small λ values, where the hard phase network is in the region of affine deformation (*SI Appendix*, Fig. S6). Another reason is that there is no strong stress concentration around the crack tip before the rupture of the hard phase network, which is seen in Fig. 3*A*.

The maximum applied energy release rate $G$ was also calculated from the work of extension of the unnotched sample (9, 30, 31). To obtain a meaningful elastic energy release rate, the hysteresis energy $U_{hys}(\lambda_{max})$ that is dissipated during each cycle by the breaking/reforming of the ionic bonds during loading is excluded from the work of extension, and $G$ was calculated from the equation $G = W_e(\lambda_{max})H_0$, where $H_0$ is the initial distance between the two clamps and $W_e(\lambda_{max})$ is the released elastic strain energy density upon unloading for the unnotched sample up to the stretch ratio $\lambda_{max}$ under the 3,000th cycle (at which the sample reached the steady state) (*SI Appendix*, Fig. S2 *B* and *C*). Even after 3,000 cycles the hysteresis loop is still very large (*SI Appendix*, Fig. S2*D*), indicating that breaking and reforming of the ionic bonds reaches a dynamic equilibrium for that applied deformation rate. Within the range of applied $G$, two characteristic crack growth modes are observed on a $\Delta c/\Delta N$ versus $G$ plot: a slow crack growth mode with a linear relation $\Delta c/\Delta N = \beta(G - G_0)$ at $G_0 < G < G_{tran}$ (Fig. 3*E*) and a fast crack growth mode after a jump at $G = G_{tran}$ (Fig. 3*F*), where $G_0$ is the fatigue threshold, below which the crack does not grow, $\beta$ is the slope of the linear response region, and $G_{tran}$ is the energy release rate at which the crack growth rate transits from slow to fast mode. $G_0$ and $G_{tran}$ correspond to $\lambda_0$ and $\lambda_{tran,}$ respectively. High $G_0$ and $G_{tran}$ as well as low $\beta$ values mean high fatigue resistance. The parameters $G_0$, $\beta$, and $G_{tran}$ extracted from Fig. 3 *E* and *F* are summarized in Table 1. The $\beta$ is reduced and $G_{tran}$ is much increased for gels dialyzed at high temperature, consistent with a high value of $\lambda_{affine}$ and a delay in fatigue fracture. The $G_0$ for these three samples is almost the same (~68 J/m$^2$). This is consistent with the reports by Suo and coworkers showing that the threshold $G_0$ is determined by the chemically cross-linked polymer network structure (9, 13, 15), which is the same for the three samples. Furthermore, $G_0$ has the same order of magnitude as

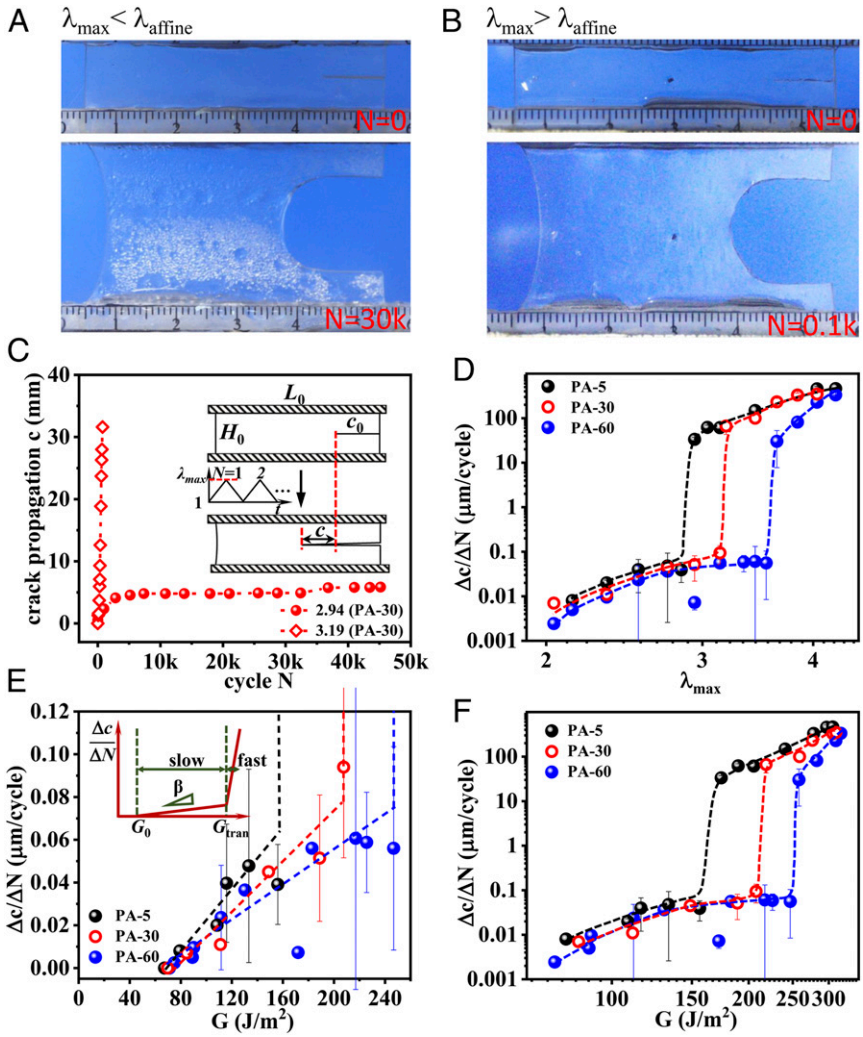


**Fig. 3.** Delayed fatigue fracture of PA gels. (*A* and *B*) Shape of crack tip for fatigue test under $\lambda_{max}$ = 2.94 (<$\lambda_{affine}$) at 30,000 cycles (*A*) and $\lambda_{max}$ = 3.19 (>$\lambda_{affine}$) at 100 cycles (*B*) for PA-30 as a representative. (*C*) Crack propagation length *c* as a function of cycle *N* at elongation ratio $\lambda_{max}$ = 2.94 and 3.19 for PA-30. (*Inset*) The geometry of the sample applied in the fatigue test (width $L_0$ = 50 mm, height $H_0$ =10 mm, initial notch length $c_0$ = 10 mm). (*D*) $\Delta c/\Delta N$ as a function of $\lambda_{max}$ for gels dialyzed at various temperatures $T_{dial}$. A transition for crack propagation from slow to fast mode is observed universally at $\lambda_{tran} \sim \lambda_{affine}$ for all of the samples. The comparison of $\lambda_{tran}$ and $\lambda_{affine}$ is shown in Fig. 2*D*. (*E*) The enlarged slow mode regime for $\Delta c/\Delta N$ as a function of energy release rate *G*. A linear relation $\Delta c/\Delta N = \beta(G - G_0)$ at $G_0 < G < G_{tran}$, is observed (as schemed in *Inset*). The $G_0$, $\beta$, and $G_{tran}$ are shown in Table 1. (*F*) The $\Delta c/\Delta N$ as functions of *G* in log-log plot. $\Delta c/\Delta N$ jumps from a low plateau (<0.1 μm per cycle) to a high value (>10 μm per cycle) at $G = G_{tran}$. The dashed lines are guides for the eyes. The average crack advance velocity $\Delta c/\Delta N$ is estimated from the slope at steady state. The $\Delta c/\Delta N$ values at the boundary of the transition regime in *D*, *E*, and *F* are obtained from the statistical average values of the high probability mode at the corresponding $\lambda_{max}$ (see *SI Appendix*, Fig. S5).

the energy required to rupture the polymer strands across the fracture plane, $\Gamma_0$, predicted by the Lake–Thomas model (32). The $G_{tran}$ is more than twice higher than $G_0$ for PA-5, and it increases to about three times and 3.5 times for PA-30 and PA-60, respectively. Since $G_{tran}$ corresponds to the maximum affine elongation ratio $\lambda_{affine}$ of the phase networks, the abrupt increase of the crack growth rate at $G_{tran}$ should be related to the breaking of the hard phase network.

**The Role of Bicontinuous Phase Networks in Antifatigue Fracture.** To investigate the effect of the bicontinuous phase networks on the fatigue-resistance behavior, we performed in situ time-resolved SAXS experiments to observe the evolution of the structure of unnotched gels under cyclic tensile deformation with the strip geometry (*SI Appendix*, Fig. S3*A*). Fig. 4 *A* and *C* show the stretch ratio of the phase networks in the perpendicular direction $d_\perp/d_0$ versus the maximum applied stretch ratio $\lambda_{max}$ at the first, third, 300th, and 1,000th cycles for $\lambda_{max}$ = 2.54 (<$\lambda_{affine}$) and $\lambda_{max}$ = 3.44 (>$\lambda_{affine}$), respectively. The PA-5 sample was adopted as an example. In the case of $\lambda_{max} < \lambda_{affine}$, the $d_\perp/d_0$ always obeys affine deformation from the first to the 1,000th cycles, except at very small λ (Fig. 4*A*). The latter should be attributed to the residual strain at unloading state. For our consecutive cyclic tensile test at a strain rate 1 $s^{-1}$, the sample has not enough time to reach full recovery when the sample approaches full unloading (*SI Appendix*, Fig. S7). The result suggests that the deformation is reversible under cyclic loading–unloading except for very small λ. This result confirms that the hard network remains intact in cyclic loading. The representative two-dimensional (2D) SAXS patterns at different λ for the 1,000th cycle are shown in Fig. 4 *A*, *Inset*. The scattering intensities exhibit a strongly elongated spot in the perpendicular direction at large deformation (λ = 2.54), suggesting the formation of highly anisotropic structure of the phase networks during the cyclic loading. It is also confirmed that no strain-induced crystallization occurs during the cyclic loading. The highly anisotropic hard strands of the intact phase

**Table 1. Comparison of fatigue parameters of PA gels with various hydrogels**

| Sample | $E^*$, MPa | $G_0$ ($\lambda_0$), J/m$^2$ | $\beta$, m$^3$/(J·cycle) | $G_{tran}$, J/m$^2$ |
|---|---|---|---|---|
| PA-60 | 0.14 | 71.1 (1.94) | $4.1 \times 10^{-10}$ | 236.2 ± 15.0 |
| PA-30 | 0.14 | 69.8 (1.94) | $6.1 \times 10^{-10}$ | 207.6 ± 0 |
| PA-5 | 0.14 | 67.3 (2.04) | $7.3 \times 10^{-10}$ | 165 ± 12.7 |
| Alginate/PAAm (13, 41) | ~0.1 | 35 (1.9) | $(1.3 \sim 2.3) \times 10^{-9}$ | 84 |
| PAAm-PVA (12) | ~0.03 | 9.5 (1.4) | $5.3 \times 10^{-7}$ | 40 |
| PAMPS/PAAm DN (14) | ~0.3 | 200 ~ 418 (~1.5) | $(1.3 \sim 4.5) \times 10^{-9}$ | — |
| PAAm (30, 35) | ~0.04 | 4.3 ~ 64.5 (~1.3) | $(0.3 \sim 3.4) \times 10^{-7}$ | — |

*The Young's modulus $E$ is tested under the same condition for the fatigue test.

network may carry, rather homogeneously, most of the stress during loading, as suggested by other oriented hard components in composite materials (17, 20, 21), preventing the stress concentration necessary for crack growth as schemed in Fig. 4*B*. This is similar to the effect of strain-induced crystallization during fatigue test in elastomers, where the hard crystal reinforces crack tip (19, 33, 34). This explains why crack blunting occurs ahead of the crack tip at $\lambda_{max} < \lambda_{affine}$ during the fatigue test in this work.

On the contrary, when cyclic loads are performed up to $\lambda_{max} > \lambda_{affine}$ (Fig. 4*C*), $d_\perp/d_0$ becomes increasingly larger with increasing number of cycles, deviating from the value predicted by the affine deformation. This suggests that the hard strands gradually rupture with increasing number of fatigue cycles, and the force-carrying ability of the hard strands decreases (*SI Appendix*, Fig. S8). Meanwhile, due to the fracture of hard strands during cyclic loading, the recovery and reassociation ability of ionic bonds with their original pairs of the virgin sample decreases, resulting in a decrease of $d_\perp/d_0$ at small $\lambda$ with cycles, as well as a more anisotropic pattern at $\lambda = 1$ after cyclic loading at $\lambda_{max} = 3.44$ ($>\lambda_{affine}$) compared with at $\lambda_{max} = 2.54$ ($<\lambda_{affine}$) (Fig. 4 *C*, *Inset*), and a much smaller hysteresis loop $U_{hys}$ at $\lambda_{max} = 3.14$ ($>\lambda_{affine}$) than at $\lambda_{max} = 2.34$ ($<\lambda_{affine}$) (*SI Appendix*, Fig. S2*D*). Once the hard strands fracture, the soft strands with sparse polymer density may carry most of the load, leading to a fast crack propagation under fatigue test as schemed in Fig. 4*D*, similar to a single network system (30, 35). That explains why we see a crack velocity jump when the maximum cyclic $\lambda_{max}$ exceeds $\lambda_{affine}$ (Fig. 3*D*).

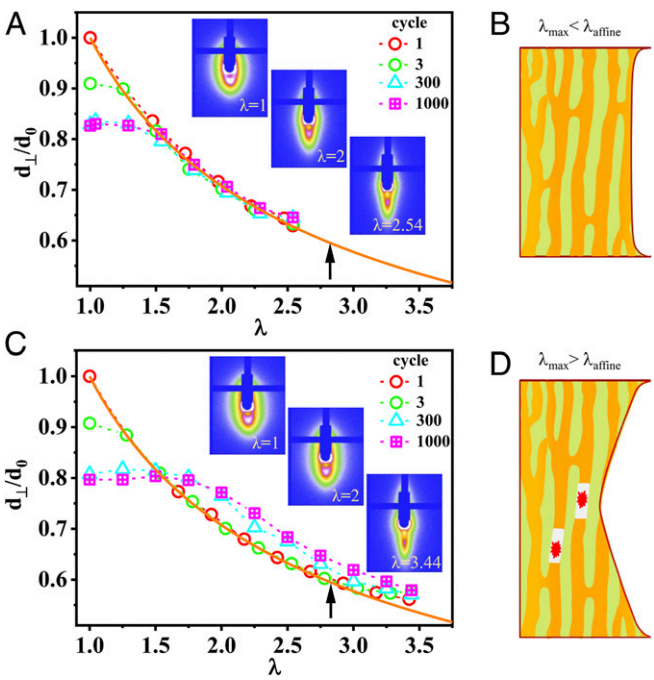


**Fig. 4.** Structure evolution of PA gels under cyclic tensile deformation. (*A* and *C*) Microscopic deformation under cyclic loading at $\lambda_{max} = 2.54$ ($<\lambda_{affine}$) (*A*) and $\lambda_{max} = 3.44$ ($>\lambda_{affine}$) (*C*) for unnotched PA-5 gel. (*Inset*) The SAXS patterns (the stretching is along horizontal direction) at representative $\lambda$ under the 1,000th cycle. The orange solid line in each figure is for affine deformation. The dashed lines are guides for the eyes. The black arrow in each figure is the maximum $\lambda$ to show affine deformation $\lambda_{affine}$. (*B* and *D*) Illustration of bicontinuous phase network deformation and rupture at $\lambda_{max}$ of fatigue test for $\lambda_{max} < \lambda_{affine}$ (*B*) and $\lambda_{max} > \lambda_{affine}$ (*D*), respectively. The red starburst pattern in *D* is the rupture of hard phase network.

To further verify the role of the hard strands for the suppression of the fast fatigue crack growth, we turned off the hard strands by preloading the unnotched sample at $\lambda_{pre} > \lambda_{affine}$ and then performed the fatigue tests immediately at $\lambda_{max} < \lambda_{affine}$ (Fig. 5*A*). The sample with ruptured hard strands exhibited the fast crack growth mode even at $\lambda_{max} < \lambda_{affine}$ (Fig. 5*B*). We also preloaded the sample at $\lambda_{pre} < \lambda_{affine}$, a stretch at which the hard strands are not damaged. This preconditioned sample showed even slightly better fatigue resistance than the pristine sample without preconditioning. These results clearly show that the presence of hard strands suppresses the fast crack growth in fatigue fracture.

Once the hard strands rupture, the PA gels with intact soft strands act as a single network gel. If we treat the dependence of $\Delta c/\Delta N$ with $G$ in the fast crack propagation regime ($G > G_{tran}$) as a linear relation, the slope $\beta_2$ is $3.1 \times 10^{-6} \sim 4.3 \times 10^{-6}$ m$^3$/(J·cycle) (*SI Appendix*, Fig. S9), close to the $\beta$ value observed for single networks of PAAm gel (Table 1). The slope $\beta_2$ slightly increases with dialysis temperature of the samples, which could be associated with the increasing degree of phase contrast of the samples prepared at high dialysis temperature (Fig. 2*A*). A higher phase contrast indicates a higher concentration contrast and a higher modulus ratio between the hard phase network and the soft phase network. The PA-60, having the relatively weaker soft phase network among the three samples, exhibits the largest exponent $\beta_2$. This result indicates that the crack grows faster with a weaker soft phase network when the hard phase network has ruptured. Such a mechanism leads to notch sensitivity of the PA gels. The prenotched sample ruptures at much smaller elongation ratio than the unnotched sample when being compared at the same pure shear geometry, due to rupture of the hard phase network (*SI Appendix*, Fig. S10).

Thanks to the role played by hard phase network in PA gels, the fatigue fracture slowed down dramatically above the threshold $G_0$. The crack advance rate $\Delta c/\Delta N$ is less than 0.1 μm per cycle and $\beta$ is as low as $10^{-10}$ m$^3$/(J·cycle) below $G_{tran}$. To see if this fatigue fracture behavior of PA gels is unique to the self-healing PA gels with mesoscale structure, we summarized the reported fatigue fracture behaviors of various hydrogels (9, 12–14, 35) (*SI Appendix*, Fig. S11 and Table 1). We see that the single-network PAAm gels and the double-network PAMPS/PAAm gels, free of physical bonds, only exhibit a single mode increase of $\Delta c/\Delta N$ above the threshold $G_0$, although in the

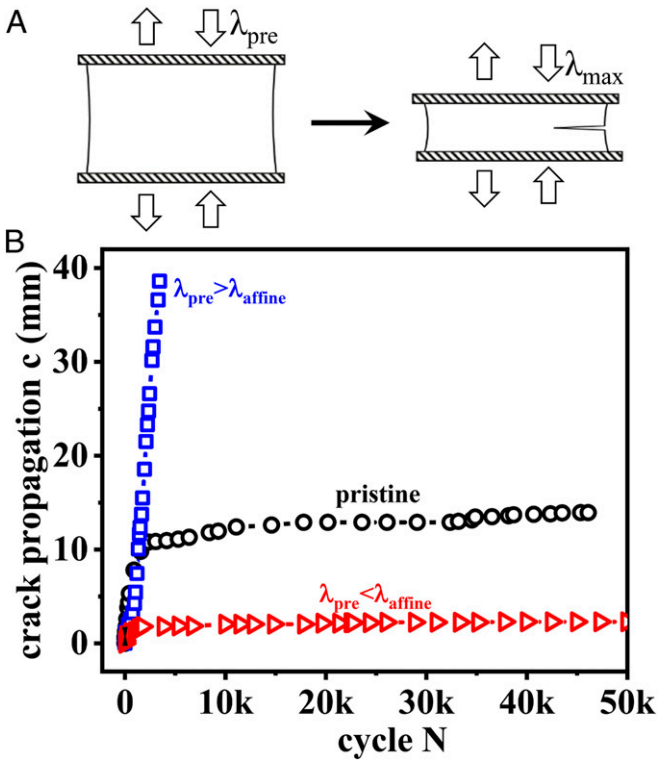


**Fig. 5.** Turning off the hard phase network and its effect on fatigue behavior. (*A*) The experimental protocol to turn off the hard phase network: The unnotched PA-5 sample is first preloaded at $\lambda_{pre}$ = 3.44 (>$\lambda_{affine}$) for 1,000 cycles, then a notch is made and fatigue test is performed at $\lambda_{max}$ = 2.54 (<$\lambda_{affine}$). For comparison, a sample with $\lambda_{pre}$ = 2.74 (<$\lambda_{affine}$) is also studied. The hollow arrows indicate cyclic loading. The single-line arrow indicates that fatigue test for notched sample is performed after the cyclic preloading. (*B*) Fatigue experimental results for samples experienced different preloading: blue, $\lambda_{pre}$ = 3.44 (>$\lambda_{affine}$) with ruptured hard phase network; red, $\lambda_{pre}$ = 2.74 (<$\lambda_{affine}$) with undamaged hard phase network; and black, pristine sample without preloading.

double-network gels the crack growth is significantly suppressed, resulting in a very large $G_0$. On the other hand, the tough and self-healing gels with physical bonds (PAAm-PVA and Ca-alginate/PAAm) also show multimode-like fatigue behaviors above the threshold $G_0$, though not as prominently as the PA gels. Especially in the case of Ca-alginate/PAAm gels with ionic cross-links, a relatively clear slow to fast crack growth transition is observed at $G_{tran} = 84$ J/m$^2$. These results suggest that these gels containing physical bonds may also contain mesoscale structure. In fact, phase separation was observed in PAAm-PVA gels (11, 36). We also see that the $\beta$ of PA gels and Ca-alginate/PAAm gels with ionic bonds is orders of magnitude smaller than the PAAm-PVA hydrogels without ionic bonds, which suggests that strong physical bonds play a role to suppress the crack growth in the slow mode regime. These results clearly show that the interplay between different scales of the gels substantially delays the fatigue crack growth.

## Conclusion

Most amorphous hydrogels exhibit extremely poor fatigue resistance. Above the fatigue threshold $G_0$, which can be predicted by the classic Lake–Thomas theory, the fatigue crack grows rapidly to cause sample failure. Thus, the fatigue threshold $G_0$ has been thought of as the most critical parameter for hydrogels under cyclic loading. In this work, we discovered that the self-healing PA hydrogels with a hierarchical structure exhibit high fatigue resistance due to the existence of multimode fatigue behaviors. The 10-nm-scale polymer network structure determines the fatigue threshold $G_0$ for the onset of crack growth, while the phase networks at the 100-nm scale, having ionic bonds at the 1-nm scale as building blocks, decelerate the advancing of fatigue crack dramatically until reaching a transition $G_{tran}$. Above $G_{tran}$, which is directly related to the rupture of the hard phase network, fast growth of the fatigue crack occurs. The synergistic effect between the structures at different length scales results in high fatigue resistance. As $G_0$ and $G_{tran}$ are related to the energy release rates at rupture of the primary network and the hard phase network, respectively, increasing the network density and rupture elongation ratios of these networks at different length scales should enhance the fatigue resistance of the materials. Furthermore, increasing the hierarchy number should induce high-order $G$ transitions with large values. The role of hierarchical structures on the delay of fatigue crack advancing elucidated in this work should guide the designing of antifatigue soft materials. It also provides clues to understanding the fatigue process of biological tissues, which have a more sophisticated hierarchical structure (37–39).

## Materials and Methods

**Materials.** The raw materials cationic monomer DMAEA-Q, anionic monomer NaSS, chemical cross-linker *N*,*N*-methylenebis(acrylamide) (MBAA), and ultraviolet initiator α-ketoglutaric acid (α-keto) were purchased from Wako Pure Chemical Industries, Ltd and used as received.

**Preparation of PA Gels.** PA gels were synthesized by a one-step random copolymerization of precursor aqueous solution containing DMAEA-Q, NaSS, MBAA, and α-keto according to previous work (25, 26, 40). The total monomer concentration is $C_m$ = 2.0 M, and both MBAA and α-keto content are 0.1 mol % (relative to $C_m$).

All details associated with sample preparations, measurement of water content, tensile tests, fatigue tests, and SAXS measurements are available in *SI Appendix*.

**Data Availability.** All data are included in the main text and *SI Appendix*.

**ACKNOWLEDGMENTS.** This work was supported by Japan Society for the Promotion of Science KAKENHI grants JP17H06144 and JP19K23617; and by ImPACT Program of the Council for Science, Technology and Innovation of the Cabinet Office, Government of Japan. The SAXS experiments were performed at the Chinese National Centre for Protein Science Shanghai BL19U2 beam line at Shanghai Synchrotron Radiation Facility. The Institute for Chemical Reaction Design and Discovery was established by World Premier International Research Initiative, Ministry of Education, Culture, Sports, Science and Technology, Japan.

1. D. Taylor, J. G. Hazenberg, T. C. Lee, Living with cracks: Damage and repair in human bone. *Nat. Mater.* **6**, 263–268 (2007).
2. O. Akkus, C. M. Rimnac, Cortical bone tissue resists fatigue fracture by deceleration and arrest of microcrack growth. *J. Biomech.* **34**, 757–764 (2001).
3. V. R. Edgerton, J. L. Smith, D. R. Simpson, Muscle fibre type populations of human leg muscles. *Histochem. J.* **7**, 259–266 (1975).
4. R. H. Fitts, Cellular mechanisms of muscle fatigue. *Physiol. Rev.* **74**, 49–94 (1994).
5. A. Huxley, *Reflections on Muscle* (Liverpool University Press, Princeton, NJ, 1980).
6. I. W. Hunter, S. Lafontaine, "A comparison of muscle with artificial actuators" in *Technical Digest IEEE Solid-State Sensor and Actuator Workshop*, (IEEE, 1992), pp. 178–185.
7. D. Taylor, N. O'Mara, E. Ryan, M. Takaza, C. Simms, The fracture toughness of soft tissues. *J. Mech. Behav. Biomed. Mater.* **6**, 139–147 (2012).
8. S. Mzabi, D. Berghezan, S. Roux, F. Hild, C. Creton, A critical local energy release rate criterion for fatigue fracture of elastomers. *J. Polym. Sci. B Polym. Phys.* **49**, 1518–1524 (2011).
9. R. Bai, J. Yang, Z. Suo, Fatigue of hydrogels. *Eur J Mech Solid* **74**, 337–370 (2019).
10. J.-Y. Sun *et al.*, Highly stretchable and tough hydrogels. *Nature* **489**, 133–136 (2012).
11. J. Li, Z. Suo, J. J. Vlassak, Stiff, strong, and tough hydrogels with good chemical stability. *J. Mater. Chem. B* **2**, 6708–6713 (2014).
12. R. Bai, J. Yang, X. P. Morelle, C. Yang, Z. Suo, Fatigue fracture of self-recovery hydrogels. *ACS Macro Lett.* **7**, 312–317 (2018).
13. W. Zhang *et al.*, Fracture toughness and fatigue threshold of tough hydrogels. *ACS Macro Lett.* **8**, 17–23 (2018).
14. W. Zhang *et al.*, Fatigue of double-network hydrogels. *Eng. Fract. Mech.* **187**, 74–93 (2018).

15. Y. Zhou *et al*., The stiffness-threshold conflict in polymer networks and a resolution. *J. Appl. Mech.* **87**, 031002 (2020).
16. C. Creton, 50th anniversary perspective: Networks and gels: Soft but dynamic and tough. *Macromolecules* **50**, 8297–8316 (2017).
17. S. Lin, J. Liu, X. Liu, X. Zhao, Muscle-like fatigue-resistant hydrogels by mechanical training. *Proc. Natl. Acad. Sci. U.S.A.* **116**, 10244–10249 (2019).
18. S. Lin *et al*., Anti-fatigue-fracture hydrogels. *Sci. Adv.* **5**, eaau8528 (2019).
19. P. Rublon *et al*., Multiaxial deformation and strain-induced crystallization around a fatigue crack in natural rubber. *Eng. Fract. Mech.* **123**, 59–69 (2014).
20. C. Li, H. Yang, Z. Suo, J. Tang, Fatigue-Resistant elastomers. *J. Mech. Phys. Solids* **134**, 103751 (2020).
21. C. Xiang *et al*., Stretchable and fatigue-resistant materials. *Mater. Today*, 10.1016/j.mattod.2019.08.009 (2019).
22. Z. Wang *et al*., Stretchable materials of high toughness and low hysteresis. *Proc. Natl. Acad. Sci. U.S.A.* **116**, 5967–5972 (2019).
23. J. J. Kruzic, Materials science. Predicting fatigue failures. *Science* **325**, 156–158 (2009).
24. J. Suhr *et al*., Fatigue resistance of aligned carbon nanotube arrays under cyclic compression. *Nat. Nanotechnol.* **2**, 417–421 (2007).
25. T. L. Sun *et al*., Physical hydrogels composed of polyampholytes demonstrate high toughness and viscoelasticity. *Nat. Mater.* **12**, 932–937 (2013).
26. A. B. Ihsan *et al*., Self-healing behaviors of tough polyampholyte hydrogels. *Macromolecules* **49**, 4245–4252 (2016).
27. T. L. Sun *et al*., Molecular structure of self-healing polyampholyte hydrogels analyzed from tensile behaviors. *Soft Matter* **11**, 9355–9366 (2015).
28. K. Cui *et al*., Multiscale energy dissipation mechanism in tough and self-healing hydrogels. *Phys. Rev. Lett.* **121**, 185501 (2018).
29. K. Cui *et al*., Effect of structure heterogeneity on mechanical performance of physical polyampholytes hydrogels. *Macromolecules* **52**, 7369–7378 (2019).
30. J. Tang, J. Li, J. J. Vlassak, Z. Suo, Fatigue fracture of hydrogels. *Extreme Mech. Lett.* **10**, 24–31 (2017).
31. R. Long, C.-Y. Hui, Fracture toughness of hydrogels: Measurement and interpretation. *Soft Matter* **12**, 8069–8086 (2016).
32. G. Lake, A. Thomas, The strength of highly elastic materials. *Proc. R. Soc. Lond. A Math. Phys. Sci.* **300**, 108–119 (1967).
33. P. Rublon *et al*., In situ synchrotron wide-angle x-ray diffraction investigation of fatigue cracks in natural rubber. *J. Synchrotron Radiat.* **20**, 105–109 (2013).
34. W. Mars, A. Fatemi, A literature survey on fatigue analysis approaches for rubber. *Int. J. Fatigue* **24**, 949–961 (2002).
35. E. Zhang, R. Bai, X. P. Morelle, Z. Suo, Fatigue fracture of nearly elastic hydrogels. *Soft Matter* **14**, 3563–3571 (2018).
36. S. Mishra, R. Bajpai, R. Katare, A. K. Bajpai, On the mechanical strength of biocompatible semi-IPNs of polyvinyl alcohol and polyacrylamide. *Microsyst. Technol.* **14**, 193–198 (2007).
37. M. A. Meyers, J. McKittrick, P.-Y. Chen, Structural biological materials: Critical mechanics-materials connections. *Science* **339**, 773–779 (2013).
38. N. Reznikov, M. Bilton, L. Lari, M. M. Stevens, R. Kröger, Fractal-like hierarchical organization of bone begins at the nanoscale. *Science* **360**, eaao2189 (2018).
39. A. Atala, F. K. Kasper, A. G. Mikos, Engineering complex tissues. *Sci. Transl. Med.* **4**, 160rv112 (2012).
40. A. B. Ihsan *et al*., A phase diagram of neutral polyampholyte–from solution to tough hydrogel. *J. Mater. Chem. B* **1**, 4555–4562 (2013).
41. R. Bai *et al*., Fatigue fracture of tough hydrogels. *Extreme Mech. Lett.* **15**, 91–96 (2017).